Geophysical Journal International

High resolution ambient noise tomography of the South-Western Alps and the ligurian margin

Journal:	*Geophysical Journal International*
Manuscript ID	GJI-S-19-0217
Manuscript Type:	Research Paper
Date Submitted by the Author:	08-Mar-2019

Complete List of Authors:	Guerin, Gauthier; Université Côte d'Azur, OCA, CNRS, IRD, Géoazur, France Rivet, Diane; Université Côte d'Azur, OCA, CNRS, IRD, Géoazur, France Deschamps, Anne; Université Côte d'Azur, OCA, CNRS, IRD, Géoazur, France Larroque, Christophe; Université Côte d'Azur, OCA, CNRS, IRD, Géoazur, France Mordret, Aurélien; Massachusetts Institute of Technology, Department of Earth, Atmospheric and Planetary Sciences Dessa, Jean-Xavier; UPMC, Géoazur Martin, Xavier; Université Côte d'Azur, OCA, CNRS, IRD, Géoazur, France

Keywords:	Structure of the Earth < GENERAL SUBJECTS, Europe < GEOGRAPHIC LOCATION, Tomography < GEOPHYSICAL METHODS, Seismic noise < SEISMOLOGY, Surface waves and free oscillations < SEISMOLOGY

High resolution ambient noise tomography of the South-Western Alps and the ligurian margin

Gauthier Guerin[1], Diane Rivet[1], Anne Deschamps[1], Christophe Larroque[1], Aurélien Mordret[2], Jean-Xavier Dessa[1], Xavier Martin[1]

[1] Université Côte d'Azur, OCA, CNRS, IRD, Géoazur, France

[2] Department of Earth, Atmospheric and Planetary Science, MIT, Cambridge, MA 02139, USA

Page heading: Southern Alps ambient noise tomography

Summary

The South-Western Alps and the Ligurian margin is a region of moderate seismicity with a high rate of small to moderate events. Identifying the active faults in this very densely populated region is critical to better assess the hazard and mitigate the risk. An accurate 3D velocity model of the shallow to middle crust is a fundamental step to better locate the seismicity, and hence, the faults from which it originates.

We performed an ambient noise surface-wave tomography based on all available continuous seismological data from the French and Italian permanent networks (RESIF, INGV, RSNI), and current and past temporary experiments (AlpArray, CASSAT, SISVAR, RISVAL). In addition to these available data, we deployed three more stations to improve the spatial resolution in a region with sparse seismic station coverage. Overall, we used 55 inland seismic stations, 5 oceans bottom seismometers and 2 offshore cabled site/sensors. Data span the 2004 – 2018 time period. Time series from all available components were cross-correlated to reconstruct both Rayleigh and Love-wave Green's functions. For each station-pair Rayleigh and Love group velocity dispersion curves were semi-automatically picked using a frequency-time analysis. Then we regionalize these group velocities to build 2D Rayleigh and Love velocity-maps between 1.5 and 9 s period. Using a two-step inversion, we estimate the best 3D shear wave velocity model. The first step is based on a Neighbourhood Algorithm to recover the best 3 layers' velocity model at each cell of the model. We then use this three-layer model as a starting model in a perturbational method based on finite elements. At periods up to 5s, the spatial variation of the velocity is well correlated with the effective geology of the area. Lower velocities are observed in areas where the sedimentary cover is thicker, such as the Var and Paillon valley near Nice, or in the subalpine domain in the northwestern part of the region. Higher velocities are retrieved in areas where massifs are present, such as the Argentera-Mercantour massifs in the northeastern, or the Esterel massif in the southwestern part of the region.

1. Introduction

The South-Western Alps-Ligurian basin junction is one the most seismically active zone of western Europe. It is presently an area of very low deformation rate and low- to moderate seismicity. Instrumental records display continuous microseismicity together with moderate-size events (ML 3.5-5) and the horizontal velocity measured from 15 years of continuous GPS is less than 0.5 mm/yr (Larroque et al., 2001; Nocquet, 2012). Nevertheless, in 1887, a major earthquake occurred 20 km offshore Impera in the Ligurian sea. It reached a macroseismic intensity of X (Medved-Sponheuer-Karnik scale) and an estimated magnitude of 6.7-6.9 (Larroque et al., 2012; Ioualalen et al., 2014). This damaging earthquake occurred in a high vulnerability area, more than 2 million people live on the french-italian Riviera between Cannes and Genoa. However, the driving mechanism of such seismicity remain poorly understood (Béthoux et al., 1992; Béthoux et al., 2008; Larroque et al., 2009). A better understanding of the origin of the seismicity would contribute mitigating the risk. In this study, we provide a regional seismic velocity model of the South-Western Alps-Ligurian basin junction that will be useful to better locate seismic events, and therefore to identify active structure which is a prerequisite to seismic hazard assessment.

Geological setting

The south-western Alps results of hundred million years of geological evolution dominated by the convergence between the Africa and Eurasia plates which led to the collision between continental blocks and to the building of the alpine mountain range from Cretaceous to Miocene times (Dercourt et al., 1986 ; Dewey et al., 1989). The south-western French Alps are now made of the high elevation Argentera massif and the southern subalpine fold and thrust belts (Tricart, 1984 ; Laurent et al., 2000) which are bounded on their western side by the Maures-Esterel Massif (Figure 1). The Argentera and Maures-Esterel massifs are composed of crystalline rocks while the southern subalpine fold and thrust belts are composed of mesozoic and cenozoic sedimentary rocks. The emplacement of the Argentera massif and the southern subalpine fold and thrust belts is related to the late phase of the alpine orogeny (~15-3 Ma, Riccou and Siddans, 1986; Fry, 1989; Bigot-Cormier et al., 2000; Sanchez et al., 2011) while the Maures-Esterel massif was mainly deformed during the hercynian orogeny and remains poorly deformed later.

During the convergence between the two plates, the Ligurian basin opened at Miocene times through this mountain range in response to the anticlockwise rotation of the Corsica-Sardinia block (Westphal, 1976; Gattacceca et al., 2007). The continental rifting started between 34 and 28 Ma and ended around 21 Ma (Réhault et al., 1984; Séranne, 1999; Rollet et al., 2002). This was followed by a drifting phase between 21 and 16 Ma. The Ligurian basin is considered to be a back-arc basin generated from the southeastward roll-back of the

Apennines–Maghrebides subduction zone (Malinverno and Ryan,1986; Faccenna et al.,1997; Jolivet et al., 2008).

The studied area can then be divided between an onshore and an offshore domain and its complex geological evolution results in an heterogeneous crustal puzzle. At depth, the Moho is located ~40–45 km below the high topography (up to 3200 m) of the Argentera and becomes shallower toward the south to reach a depth around 27 km below the coast (e.g. Masson et al., 1999; Thouvenot et al., 2007; Schreiber et al., 2010, Stehly et al. 2009). The northern ligurian margin is narrow and the continental crust thins abruptly in a few tens of kilometers from the coast and, in the basin, the oceanic crust is 4 km in thickness (Chamoot-Rooke et al., 1999; Rollet et al., 2002).

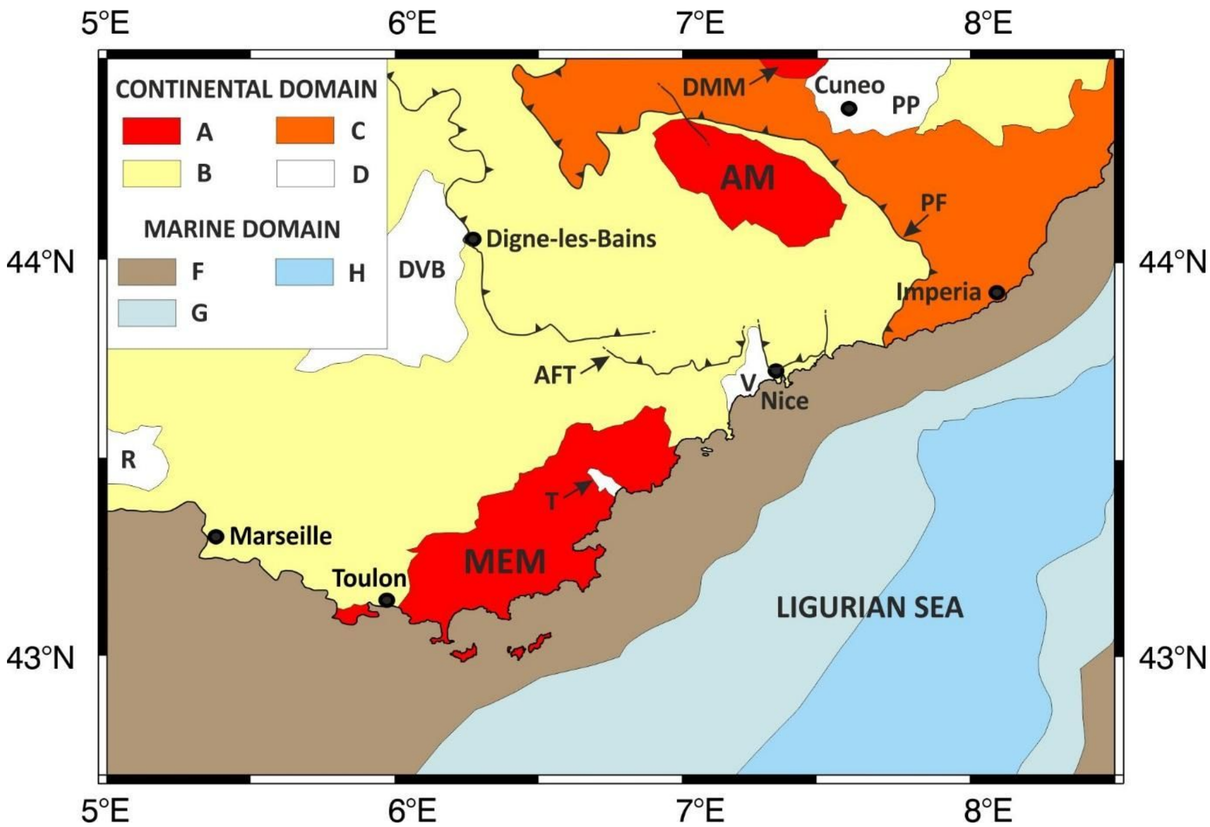

Figure 1. Simplified geological map of the South-Western Alps - Ligurian sea area (from Carte Géologique de France, BRGM and Rollet et al., 2002) . Continental domain : A, Palaeozoic crystalline basement (AM : Argentera Massif, DMM : Dora Maira Massif, MEM : Maures-Esterel Massif); B, Meso-Cenozoic sedimentary cover of the external alpine belt; C, sedimentary cover of the internal alpine belt; D, Plio-Quaternary sedimentary deposits (DVB, Durance-Valensole basin; PP, Po Plain; V, Var basin; R, Rhone basin; T, Tanneron basin); AFT, Alpine frontal thrust; PF, Penninic front

(internal alpine thrust). Marine domain: F, thinned continental crust of the Ligurian margin; G, transitional oceanic-continental crust; H, oceanic crust.

Ambient noise tomography

Ambient noise tomography is based on the reconstruction of the Green's function between different receivers from the cross correlation (CC) of long duration ambient noise records. In the 1 to 10 s period band, ambient noise tomography allows us to gain insight into the first tens of kilometers of the subsurface. Numerous ambient noise surface wave tomography has been performed at regional scale in densely instrumented areas [e.g., Lin et al., 2007; Stehly et al., 2009; Mordret et al., 2014; Giannopoulos et al., 2017; Schippkus et al., 2018;]. Regional seismic velocity models are important for seismic hazard assessment because they contribute to a better location of the seismic events and highlight the relationship between the seismicity and the crustal structures. Because surface wave tomography allows building a precise velocity model for the shallow and the middle crust, it also helps to better retrieve, on one hand, deeper discontinuities and structures in the deep crust and shallow mantle using body waves tomography (e.g., Rawlinson and Fishwick, 2012; Nunn et al., 2014) and, on the other hand, serve as a reference model to study shallow structures (e.g. above 1 km depth) such as shallow sedimentary basin using geotechnics methods.

Over the past 10 years, the development of dense permanent seismic networks with high quality broad-band stations (RESIF-RLBP, GU, INGV) in the South-Western alps – Ligurian allows to study the crustal structures with a high resolution. In addition to further increase the resolution we use continuous data recorded during current and past temporary experiments. This multiplication of deployed stations allows us to break away from the uneven spatio-temporal distribution of seismicity using the ambient noise tomography.

At the scale of the whole Alpine continental collision zone, Kästle et al. [2017] and Lu et al. [2018] recently performed ambient noise tomography to image the velocity structure from the middle crust to the upper mantle and the Moho depth. Here, we present the tomography of South-Western Alps/Ligurian Sea by using Rayleigh, Scholte and Love's waves altogether. First, we estimate Rayleigh, Scholte and Love wave group velocity maps from the dispersion curves of ambient noise cross-correlation. We then invert for the shear velocity at depth from the regionalized Rayleigh and Scholte wave group velocities.

2. Continuous seismological data

We used continuous seismic ambient noise records of short-period and broad-band sensors of the French (RESIF (1995) – 28 stations) and Italian (INGV Seismological Data Centre. (1997) – 8 stations, Regional Seismic Network of Italy – 6 stations) permanent seismic networks as well as 18 temporary stations set up for past or current experiments (*AlpArray Seismic Network (2015)* - Hetenyi et al. (2018)), POSA (French National Research Agency ANR), CASSAT, SISVAR and RISVAL (European Alcotra programs). In addition, data from 5 ocean bottom seismometer from AlpArray-Ligure program deployed during 2 months in 2017 and 2 off-shore cabled seismometer from European EMSO-Ligure program have been used to image the French part of the Ligurian Sea. Lastly, we installed 3 temporary stations during 3 months in order to increase the resolution in the western part of our velocity model where the permanent stations coverage is less dense. Overall, we used continuous seismic noise of 62 stations across the Southern Alps and the Ligurian Sea between 2011 and 2018. In this study, we select seismic record range goes from 3 months up to 1 year in length. Among these stations, 12 are single-component stations. The interstation distances range from 500 m in the Var valley to 250 km between Italy and France. Figure 2 shows an overview of the study area and the locations of the stations.

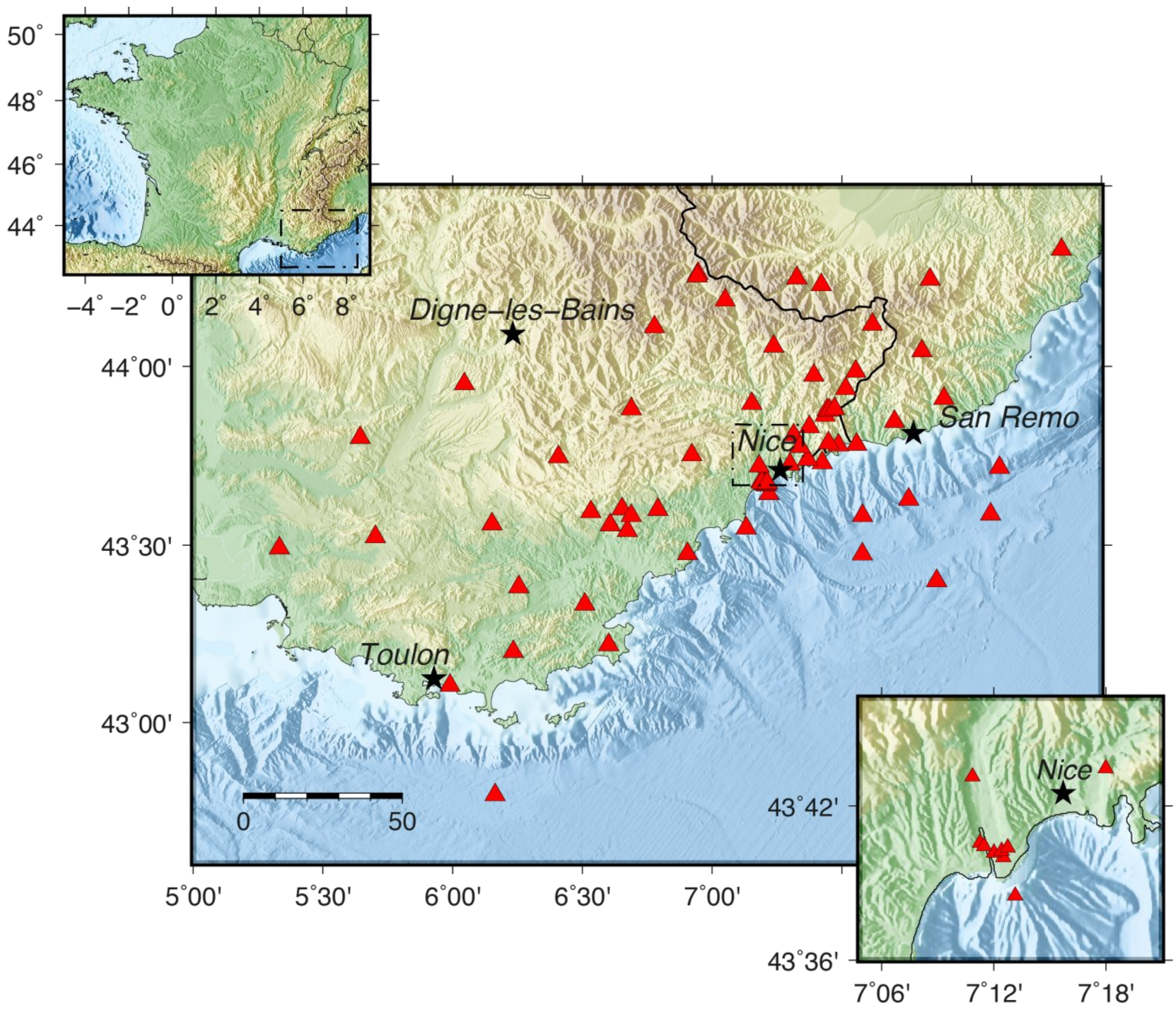

Figure 2. Map view of the south-western Alps and the Ligurian margin with the location of the 62 stations used in this study. Only 2 are short-band stations. The black stars indicate the main city. The region shows a high topography gradient from -2500m in the Ligurian basin to 3300m in the Argentera-Mercantour Massif distant of 70 km.

3. Ambient noise surface-wave tomography

Seismic noise cross-correlation

We performed the ambient noise tomography of the South-Western Alps following the approach developed by Ritzwoller & al., (2011) and Mordret et al., (2014). The first step consisted in retrieving empirical Green's functions between all station pairs from CCs of ambient seismic noise and measuring the frequency-dependent group travel times from every station pair CC. Then, we built 2-D group velocity maps at each period by inverting the surface wave travel times. Lastly, we inverted both Rayleigh and Love-wave group velocity maps, with the aim of deriving the structure at depth inverting dispersion curves for a 1-D shear-velocity model in every cell of the grid. The latter was performed by using two different methods described afterwards. One of specific features to take account for depth inversion is that ambient noise at the seafloor is composed of Scholte waves which are surface waves found at interface between rock basement and sea. The presence of a water layer in a model makes that the guided Scholte waves are slower at the same frequency compared with the surface's waves.

Pre-process and cross-correlation computation

In order to obtain the most stable Green functions (GF), a pre-processing was applied on all raw data following Bensen & al. (2007). The first step consists in removing the mean and the trend of the signal, bandpass filtering between 0.02 and 2.5 Hz, decimating the signal to 5 Hz, and removing the instrument response. The second step aims at removing glitches and earthquakes by clipping amplitudes greater than 10 times the standard deviation estimated daily. Then a spectral whitening between 0.02 and 2.5 Hz was applied before removing part of the signal with amplitudes greater than 3 times the standard deviation. Finally, a one-bit normalization was applied. This procedure is common for that type of study and applied to all single day of continuous seismic recordings.

From the pre-processed daily time series, we computed all the cross-correlations for Z, N and E components for each station pair (ZZ, NN, EE, EN, NE). We rotate the cross-correlation tensor to retrieve radial-radial (RR), radial-transverse (RT), transverse-radial (TR) and transverse-transverse (TT) components to recover both Rayleigh and Love waves (Lin & al., 2008). The ZZ, RR, ZR, and RZ components of the cross-correlations are used to estimate Rayleigh waves velocity, while the TT component is used to estimate Love waves velocity. However, in order to estimate Rayleigh waves velocity only the ZZ component of the cross-correlations are used because it has a significantly higher signal-to-noise ratio (SNR) than RR, ZR and ZR counterparts.

To improve SNR, we finally stacked all daily cross-correlations for all available periods and merged the two-sided signal into a one-sided one by averaging positive and negative lag times. Most of the CCs with SNRs greater than 1.5 are found for station pairs located between 10 and 80 km apart.

Dispersion measurement

After getting the estimated Green function from each station pair, we can retrieve group velocities of surface waves by using traditional frequency-time analyses (FTAN) [Levshin et al., 1989]. Given the number of CCs extracted (more than 3000), group velocity dispersion curves are commonly picked automatically. However, dispersion curves having a low SNR due to high-amplitude surface wave overtones or scattered waves in the signal are picked manually, thanks to a Graphical Users Interface developed by Mordret & al. (2015). It allowed us to select the best dispersion curves and mitigate above-mentioned effects. We used both Love and Rayleigh waves to see if there are structures affected by significant radial anisotropy in this area, revealed by strong differences between the horizontal and vertical shear velocities. Figure 3 presents the Rayleigh wave extracted from the cross-correlation between A206A-LEPF and the dispersion of the group velocity, with phase velocity increasing with period.

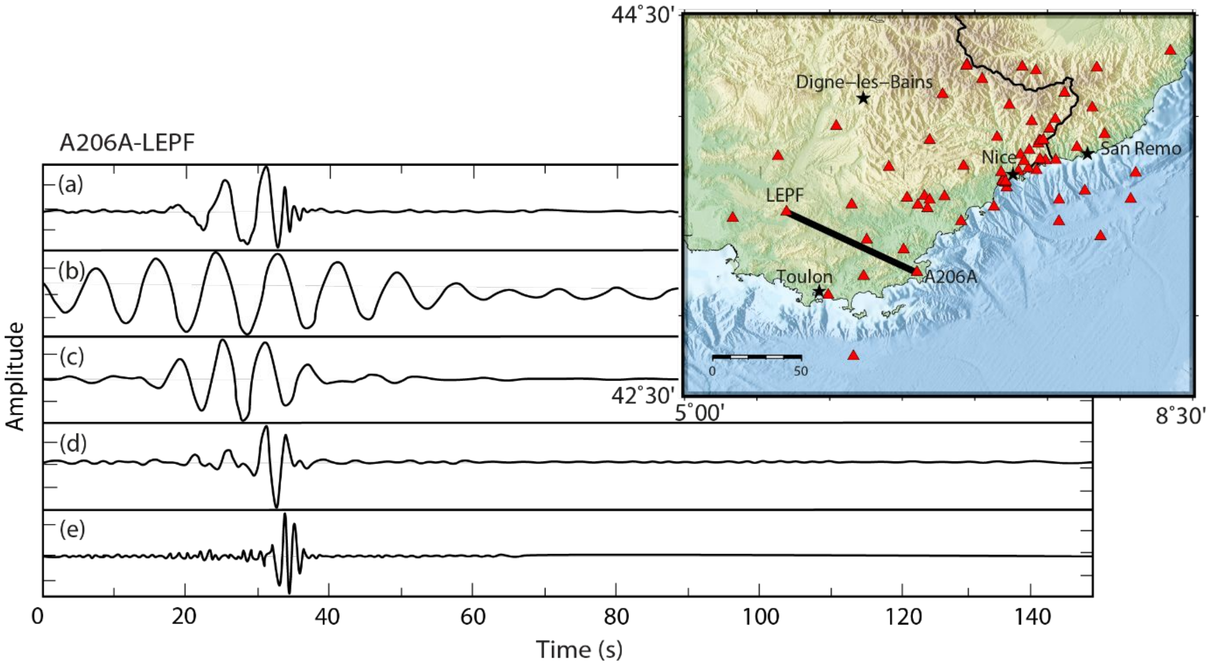

Figure 3. Cross-correlation between A206A-LEPF filtered for several labelled period bands and computed for the ZZ components of ambient noise. (a) Broad-band signal (0.4-14 s passband), while filtered signal is shown below with (b) 8-10 s, (c) 5-8 s, (d) 2-5 s, and (e) 0.4-2 s. Black curve on the map indicates the path A206A-LEPF. Inter stations distance is 80 km.

Figure 4a shows the cross-correlation surface-waves on which the picking has been done to retrieve group-velocity as a function of periods. Figure 4b shows period-velocity diagrams for the station pair A206A-LEPF (80 km interstation distance) for the three ZZ, RR and TT components. The frequency-time diagrams use the dispersion of the surface wave to obtain group-velocity measurements. The black dots correspond to the relative maxima of the diagrams whereas the white circles show the manually validated maxima corresponding to the fundamental mode. The latter are interpolated and smoothed by a fifth-order polynomial represented by the black curve.

We noticed that ZZ and RR component dispersion curve are picked in the same periods range and exhibit almost similar speed. On the other hand, the TT dispersion curve seems to show velocity faster than for the Rayleigh's wave component. Because many stations were temporary stations the RR components got the least amount of energy and have a lower

SNR (Fuchs et al. [2015]). Therefore in the following we consider only the ZZ dispersion curve to invert of the Rayleigh wave group velocity map.

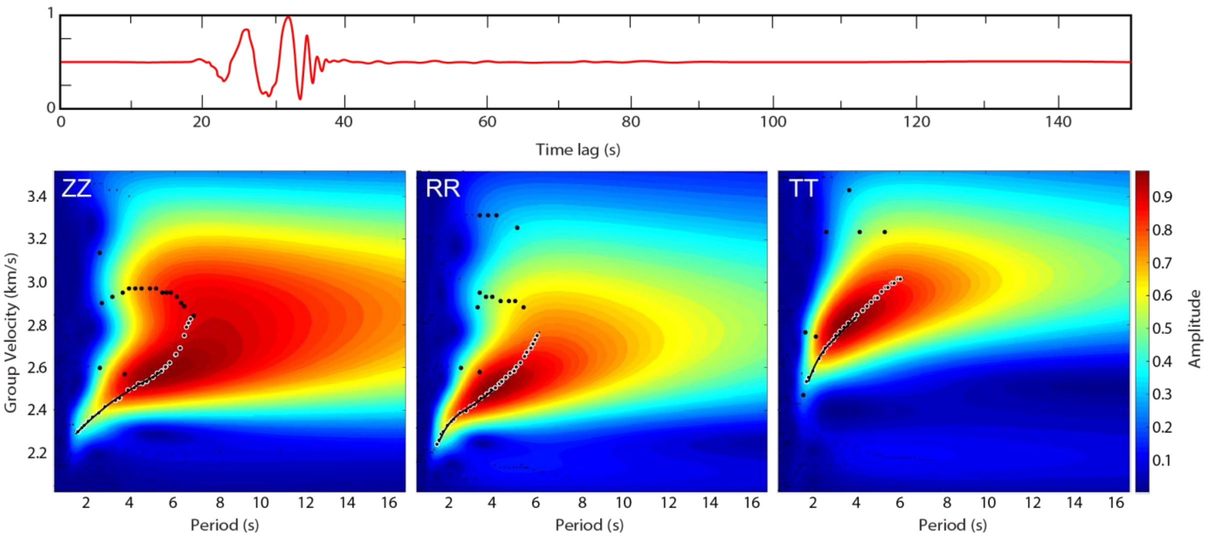

Figure 4. (a) Cross-correlation between A206A-LEPF pair station for ZZ component. Red signal represents the correlation. (b) Example of dispersion curve picking on the frequency-time for all three-components ZZ, RR and TT. Warm colors showing the maxima of energy in the signal. Black dots represent the relative maxima of the diagram for the instantaneous frequency. White circles highlight the automatic picking of these points. The black line is a five-order polynomial fitting to the automatic picks.

The number of dispersion curves picked as a function of periods for ZZ and TT components is presented in Figure 5a. The error bars present the standard deviation of the mean dispersion (red curve) at each period. For the same reasons that RR component (low SNR), we picked less TT component dispersion curve number than ZZ. Overall, we noticed that our ZZ and RR components seems to have similar lowest speed, as compared to TT components (Figure 5a). We can observe that most of the dispersion curves are in range from 2 to 8 s periods with a deterioration of quality above 9 s and below 2 s. We retrieve a total of 1206 usable GF's from ZZ component, 923 from TT, each of them having a different period range. A summary is presented on the Figure 5b.

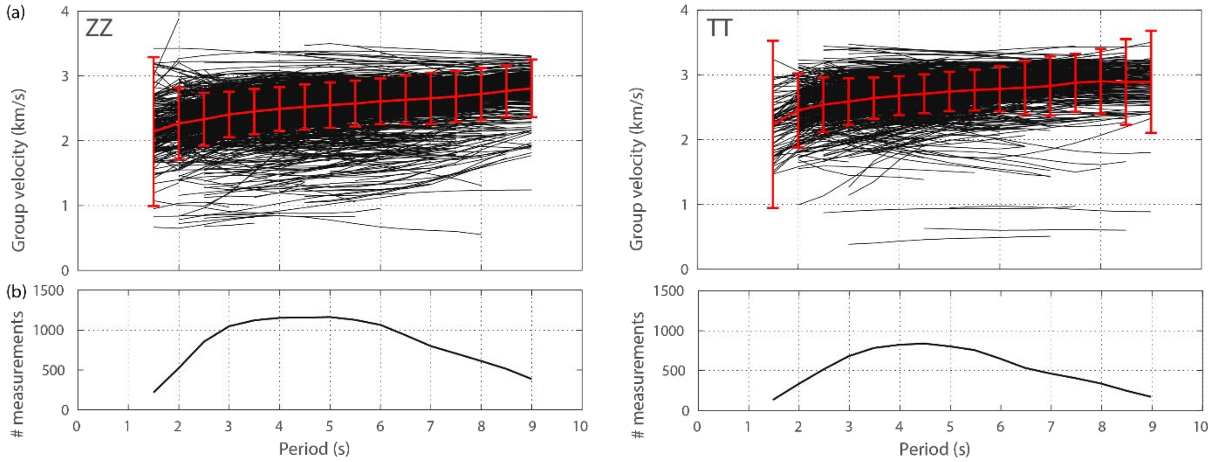

Figure 5. (a) All measured Rayleigh and Love-wave dispersion curves are plotted on a group velocity-period diagram. The average dispersion curve with its standard deviation is plotted as red line. (b) Diagram representing the number of measurements with respect to period for ZZ (left) and TT (right).

Rayleigh-wave group velocity maps

Group velocity maps are generated using the method of Barmin et al. [2001] which is based on ray theory involving a regularization function. This function is composed of a spatial Gaussian smoothing function and a constraint on the amplitude of the perturbation depending on local path density. We used a Cartesian version of this algorithm which is described for this study described by Mordret et al. [2013]. We performed two successive inversions to regionalize surface wave group velocities over a 22 x 38 grid, with a cell size of 9.45 km x 6.95 km. The first inversion computes an overdamped model with all paths to remove outliers. For this purpose, we discard all paths for which the difference between the measured travel time (Figure 6) and the travel time computed during the first inversion is greater than twice the standard deviation. Overall, they represent less than 5% of the selected paths. The second inversion is performed with the optimal smoothing and damping parameters. The cells of the model with less than 4 rays are discarded.

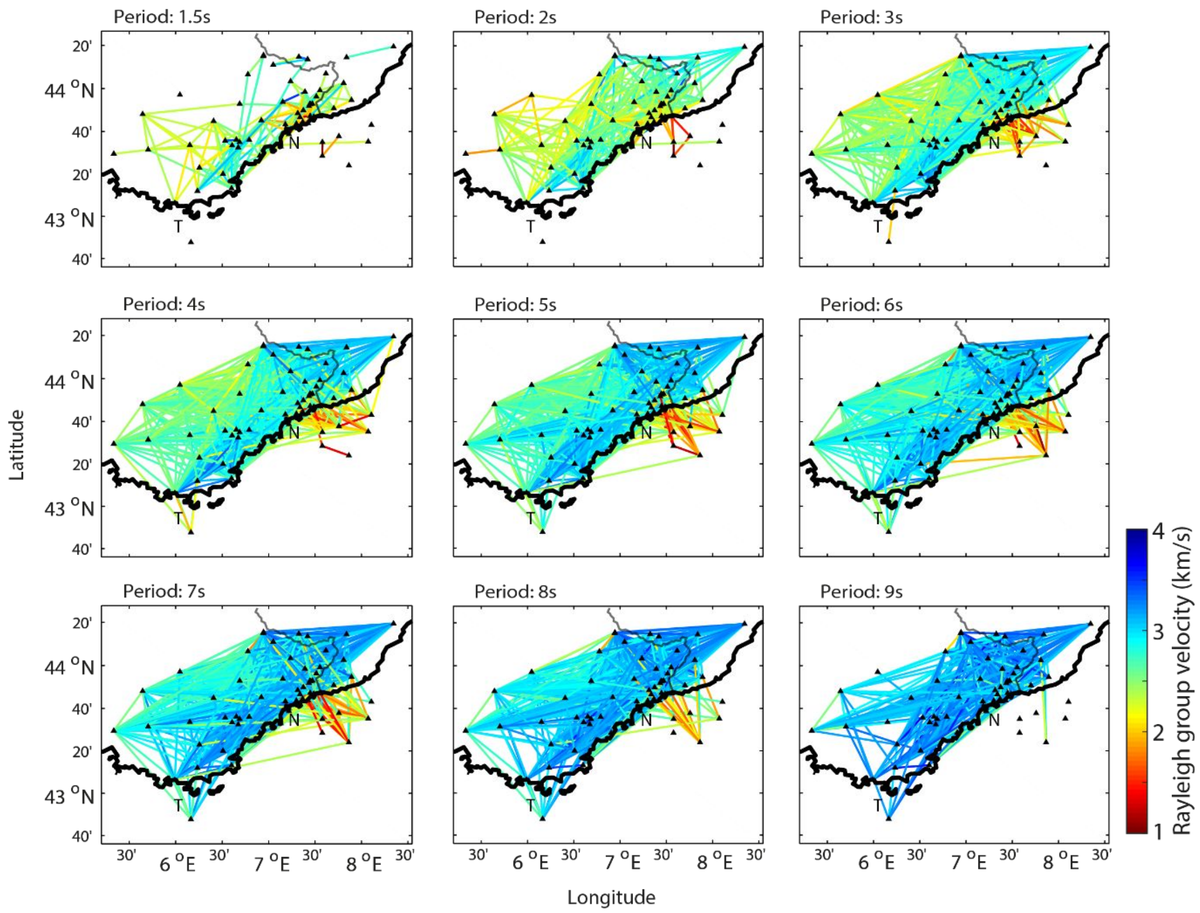

Figure 6. Rayleigh-wave group velocity measurements for ZZ components and associated ray-path coverage to periods from 1.5 to 9 s. Seismic stations are shown as black triangles. T indicates the city of Toulon. N indicates the city of Nice. Grey curve shows the Franco-Italian border.

We inverted both measured Rayleigh and Love wave dispersion curves group velocity map at 16 periods with a step of 0.5 s between 1.5 and 9 s. We do not take into account the topography during the inversion procedure. Most of our interstation paths with large topographic contrast correspond to long distances with mostly sensitivity at long periods. As shown in Köhler et al. [2012], the topography effect at long distances, is averaged out by 3-D effect, and its impact on wave velocity measurements is negligible.

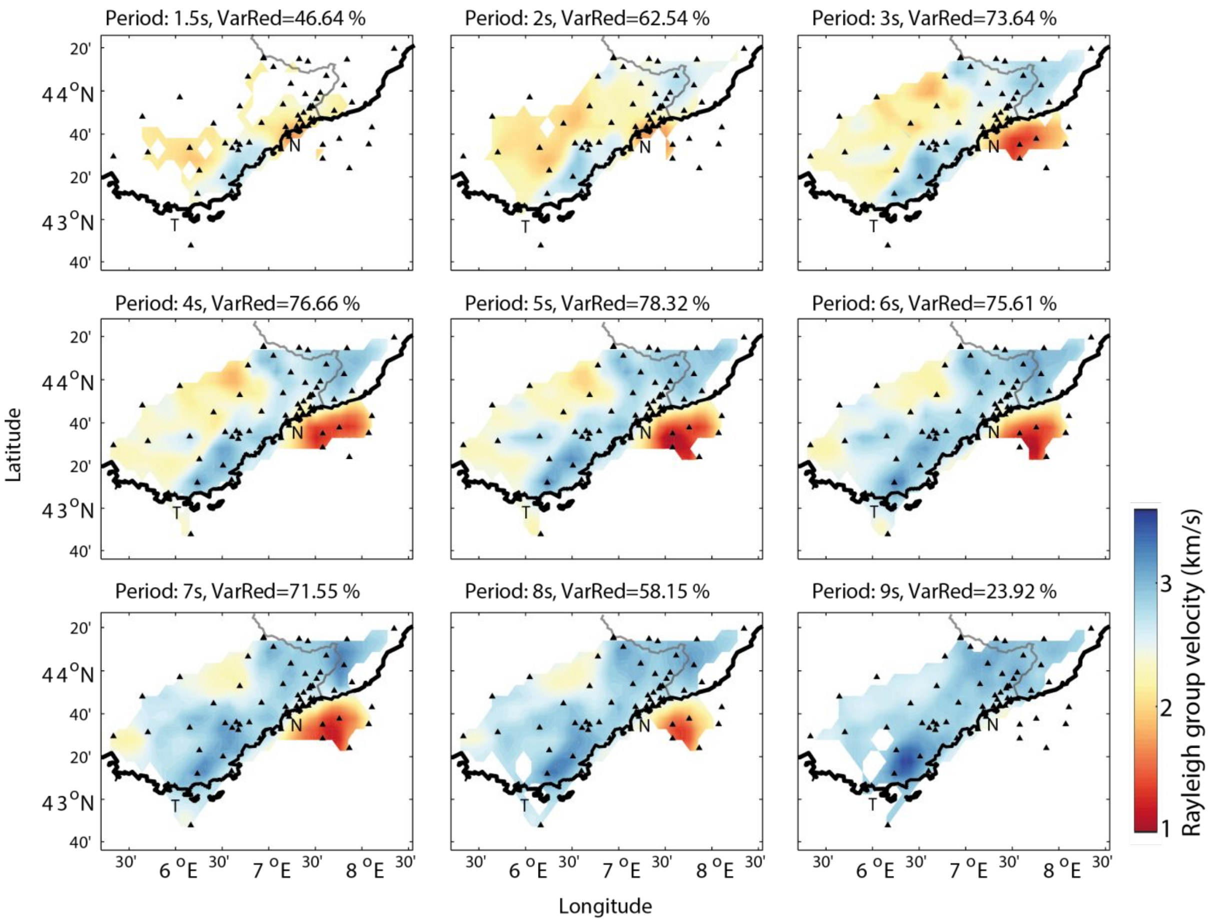

Figure 7. Rayleigh wave group-velocity maps for 1.5, 2, 3, 4, 5, 6, 7, 8, and 9 s, respectively. At each period, we indicated the variance reduction (VarRed) between data computed from the measurement and the final model. The black bold curve shows the coastline while the grey curve indicates the Franco-Italian border. Seismic stations are shown as black triangles. T indicates the city of Toulon. N indicates the city of Nice.

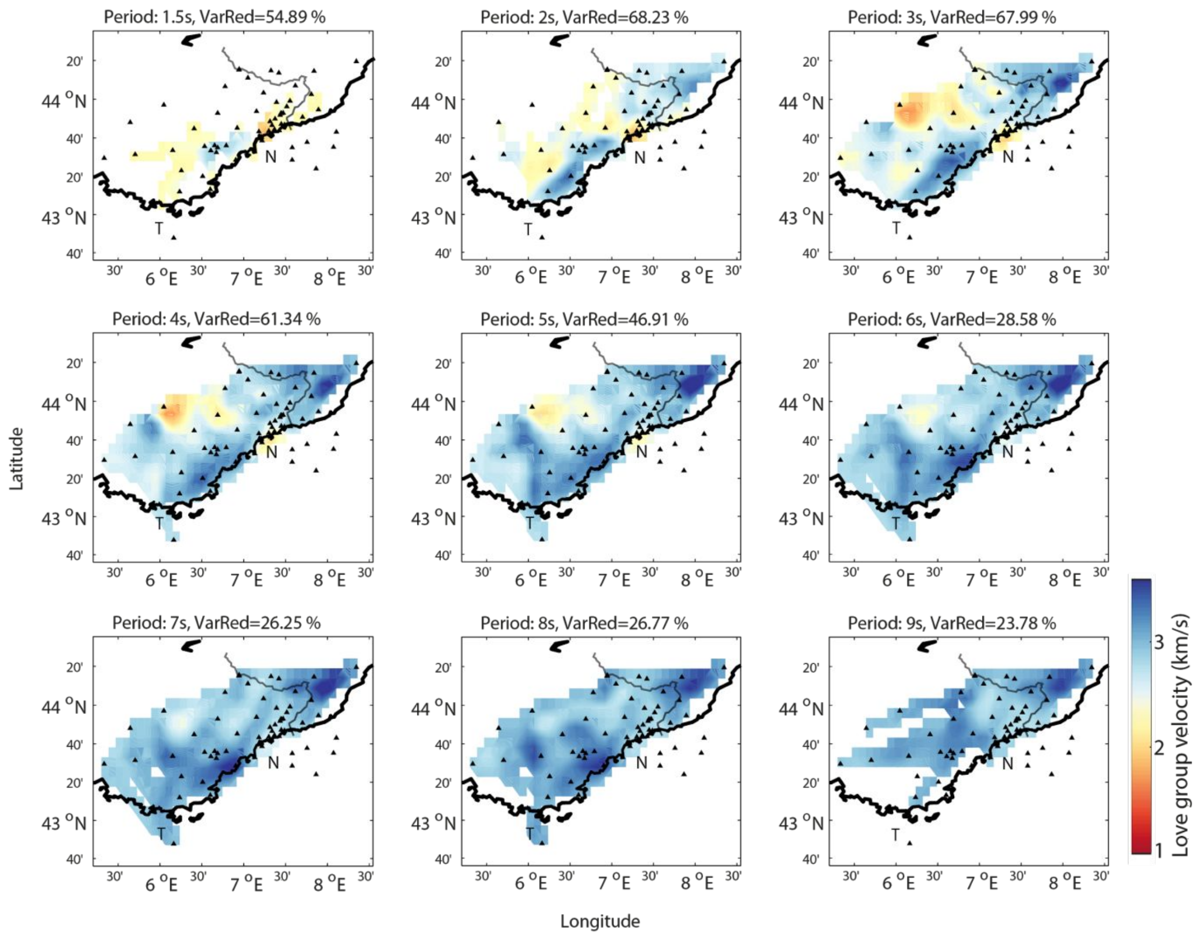

Figure 8. Same as figure 7 but for Love wave group-velocity maps for 1.5, 2, 3, 4, 5, 6, 7, 8, and 9 s, respectively.

We present our final group velocity maps for both Rayleigh and Love waves group velocity at range periods from 1.5 to 9 s with a step of 0.5 s (resp. Figure 7 and Figure 8). The mean variance reduction of the travel time residual shows values around 50% indicating that those velocities models fit well. If we compare group velocity map at each period for the ZZ and TT components, we can notice that Love wave velocity is on average higher for all identified structures.

On both Rayleigh and Love group velocity maps, we observe two high-velocity anomalies in the northeastern and southwestern part corresponding, respectively to the Mercantour Argentera Massif - Briançonnais zone and the Esterel-Maure massif. We identify a low velocity anomaly area around Nice and overall on the coastline. A localized low velocity anomaly centered on the Var Valley (V on figure 1) is clearly observed on the Love group velocity map up to 4 s. A large low velocity anomaly zone is observed up to 8 s on the northwestern part of both the Rayleigh and Love group velocity maps, spatially correlated with a Subalpine thrust mass with Cretaceous and Jurassic carbonates, with lowest velocity centered on the Valensole plio-quaternaire bassin (VSB). Lastly, on the Rayleigh group velocity maps the lowest velocity anomaly is observed in the Liguria sea for each available period, which is consistent with Scholte surface wave velocity.

Resolution

It is essential to assess the spatial resolution of each group-velocity maps to estimate their geometrical accuracy. In our main study area (the southern termination of the Alps), where station coverage is very dense, we got on average more than 80 paths per cell. In this case, the resolution length is expected to tend towards the model's cell size. In the western, and easternmost areas, the low station density as well as the fact that the majority of paths exhibit large interstation distances (lowest SNR at 4s) yields an expected loss in spatial resolution.

Figure 9a shows the average resolution at 4 s, estimated from the resolution matrices [Barmin et al., 2001; Mordret et al., 2013]. The resolution matrix is the response of the tomographic process to a Delta function type anomaly located in a corresponding cell of the model. It indicates how accurately the tomography is able to retrieve the anomaly. Overall, in our 2-9 s period band, the resolution of the group velocity map is good with a maximum of 35 km wavelength at the limit of our study area. From the Var to the Italian border, where ray coverage is dense, the spatial resolution decreases to around 10 km wavelength. Figure 9b represents the resolution shift which is the actual position of the spot with respect to its theoretical position and it shows if the observed anomalies are at the right position on the map. Nearly all the shift resolution is ranging between 0 and 5 km, which means that the retrieved anomalies are located in the good cell.

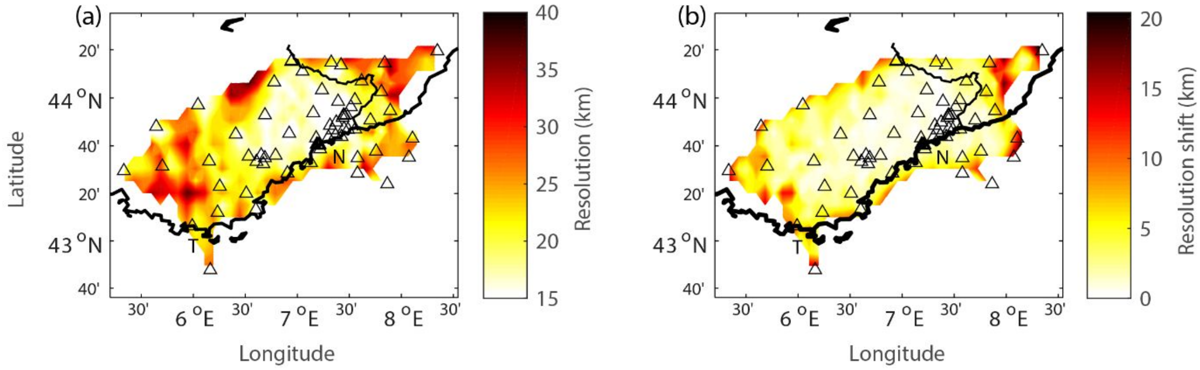

Figure 9. (a) Spatial resolution map for Rayleigh waves at 4 s. (b) Resolution shift map for Rayleigh wave at 4 s. For the two figures, the black bold curve shows the coastline. Seismic stations are shown as black outline triangles. The black bold curve shows the coastline. The thinner black curve indicates the Franco-Italian border.

Shear-velocity inversion

Rayleigh and Love-wave group velocity maps provide information about lateral variations of surface wave velocities with respect to the period. In order to obtain insight into the structure at depth, we extract all available local regionalized dispersion curves to construct a local 1-D shear velocity model. Then, we combine all those 1-D profiles from all cells to construct the final 3-D shear velocity model. As a reminder, we used a 22 x 38 grid with a cell size of 0.085° x 0.085°.

As mentioned previously, we performed a two-step inversion. The first inversion is based on the Neighborhood Algorithm, an optimized Monte-Carlo global search technique developed by Sambridge (1999a,b) to sample a model-space, which has been efficiently deployed in different geophysics inversions (e.g. Mordret et al. 2014, 2015; Giannopoulos et al. 2017). A model is a set of different parameters and the corresponding model-space is a multidimensional space having the same dimensions as the number of the parameters used to characterize the model. For each parameter of our model-space, we fixed an a priori range of value. Hence, for our local DC inversion problem, the model is a 1-D layered shear-wave velocity profile with two parameters for each layer, the thickness and the S-wave velocity. For the two following inversions, we take in account that ambient noise at the ocean floor is composed of Scholte wave. More information about the methodology features in Mordret et al. (2014).

All our local 1-D shear velocity model are based on an initial model with three layers over a half space with five unknowns: three S-wave velocities and the depths of two interfaces separating them. More than 27000 models have been sampled for each cell during this inversion. Figure 10a,b,c shows the 1D dispersion curves with the red errors bars derived from the initial measured dispersion curves, and on which the depth inversion is computed. We average the 100 best models to get the final model which corresponds to the red curves in Figure 10d,e,f. The other colors curve indicates all the models sampled. The misfit of the best model is on average lower than 0.01. This three-layer depth inversion allows to identify major features of the studied region. As an example, we computed three models which have specific S-wave velocity anomalies. Figure 9a and 9c show high anomalies that correspond respectively to the crystalline Mercantour-Argentera massif and a part of the Maures massif and Figure 9b shows a lowest velocity anomalies zone around Nice and the Var valley with thick sediment deposits. We can notice two similar patterns corresponding to the Argentera-Mercantour (Figure 10d) and the Maures massif (Figure 10f), with a first layer exhibiting a shear wave velocity of ~2.4 km/s at 2 km depth, a second layer up to 5-7 km depth with ~ 2.8 km/s velocity and lastly, a ~3.4 km/s velocity found in the third layer. From the known geology of the area, we can assume that the sedimentary cover lies between the surface and the first layer, then a second layer corresponding to the crystalline substratum. When looking at the second location (Fig. 10b) corresponding to an area between Monaco, Nice and the Var Valley, we can see a first 1 km deep layer of ~1.9 km/s S-wave velocity underlied by a second one with a mean velocity of ~2.1 km/s down to 3 km depth. Given the number of stations in this area, a good part of the short period (< 2 seconds) were picked and therefore we have a better resolution to image the superficial crust.

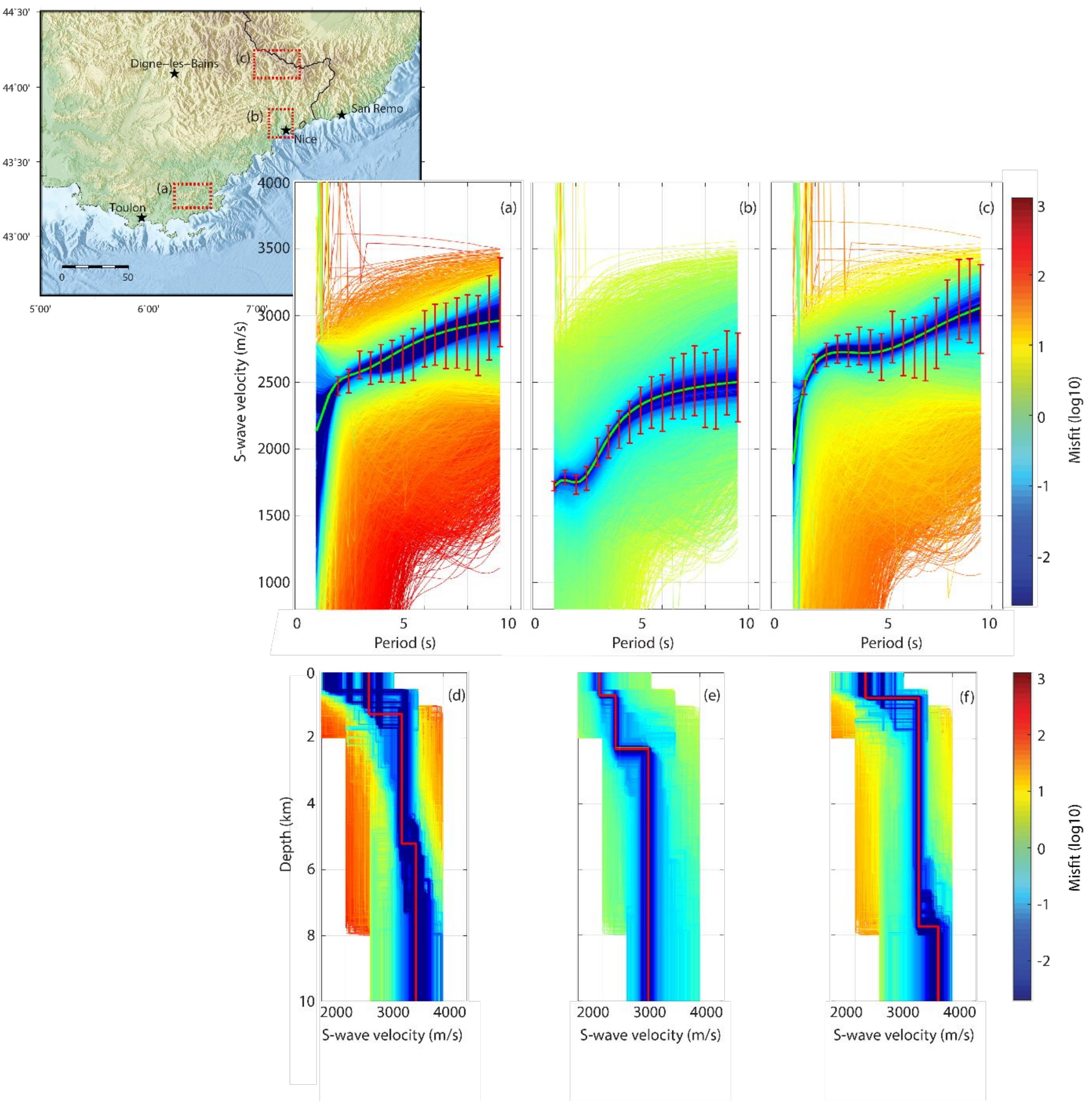

Figure 10. Inverted shear wave velocity model for specific locations in our study area: (a) and (d) feature the Mercantour-Argentera massif (rectangle a in the inset map) ; (b) and (e) an area around the Var (rectangle b in the inset map); (c) and (f) is the eastern part of the Maures massif (rectangle c in the inset map). (a), (b), (c) show in red the error bars of the regionalized 1D Rayleigh waves dispersion curves from which the shear wave inverted models are computed, in color-coded the computed Rayleigh waves dispersion curves with respective misfit, and the green lines featuring the models with minimum misfit. (d), (e), (f) shows the associated inverted models with color-coded misfit,

the red lines representing the best fitting model. Our final model is taken as the average of the 100 best models, with the lower misfit.

We then perform a second inversion based on a perturbational method using finite elements (Haney and Tsai (2017)). The individual finite elements, or layers, must be thin compared with the wavelength to ensure accuracy. Here, the frequency is fixed while the wavenumber and material properties are perturbed. It yields a first-order result relating perturbations in phase/group velocity to perturbations in the material properties.

This second inversion allows to refine the depth-dependent Vs profiles with a finer depth discretization of the models. As inputs, we use the three-layer model generated previously as well as the 1D dispersion curves. Here, a multi-layer parameterization with different thicknesses is considered, instead of merely three layers. It exists an optimal depth discretization with an increasing thickness in depth. A such layering allows us to properly sample the Rayleigh waves at any depths. This optimal layering for Rayleigh-wave modeling is based on a phase velocity dispersion curve. Following Haney and Tsai (2017), we find that our optimal number of layers is around 40 on land, and 30 at sea. The total depth of the model is 30 km, allowing to recover good accuracy in the first ten kilometers depth. As 2 smoothing factors, we set the smoothness scale at 3 km (half-space depth), and the model standard deviation factor at 4 for every cell. Considering the sensitivity depth of the Rayleigh Wave with periods, most of the layers are sampled in the upper third of the model. In Figure 11a shows an example of dispersion curves on which models are generated for a cell located below Nicew. Given that the first inversion misfit is good, we decided to lower the velocity values errors by a factor 2 (black error bars in Figure 11a). We noticed that the second inversion improve the misfit, especially at low frequencies. The final update (red curve) predicts overall more than 95 % of the group velocity measurements. We generated the models with a chi-squared value below 1. In Fig 11b, the corresponding three-layer (green curve) and multi-layers (red curve) models resulting from our successive inversions.

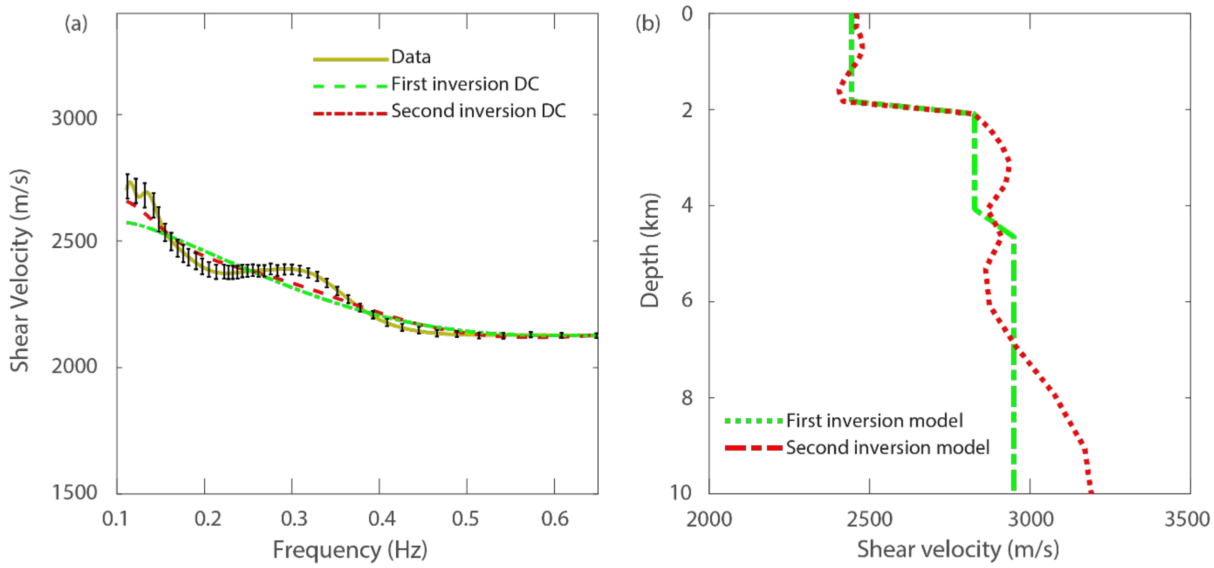

Figure 11. (a) Group velocity dispersion curves for the cell below the city of Nice: data from dispersion measurement (yellow), synthetic DC from the three-layer model (green), and from the multi-layer model (red). (b) Shear velocity depth models using group velocities: initial three-layer model (green) and final multi-layer model (red). The black error bar is computed the same way as the first inversion but divided by a factor of 2. Chi-squared is less than 0.5 for this cell.

The final step consists in collecting the best-fitting 1D depth profiles for each grid cell and in generating a 3D shear-velocity model of the south-western Alps and Ligurian margin. In Figure 12 we present selected depth (600, 2000, 3800, and 6400 m) slices of our final 3-D shear-velocity model.

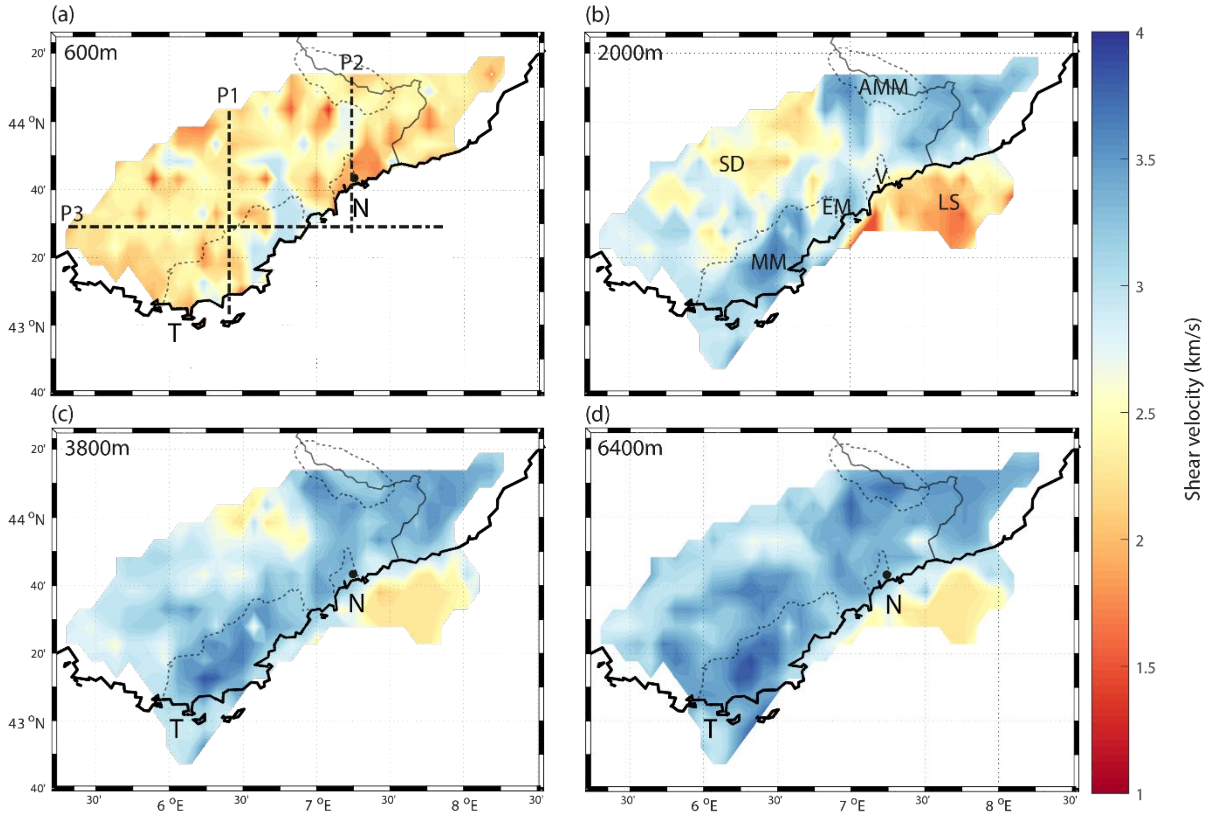

Figure 12. Depth slices through the 3-D final shear-velocity models at (a) 600 m, (b) 2000 m, (c) 3800 m and (d) 6400 m below the sea level. Major toponyms and areas are labelled: T, Toulon; N, Nice; V, Var; SD, Subalpine Domain; AMM, Argentera-Mercantour Massif; MM, Maures Massif; EM, Esterel Massif; LS, Ligurian Margin. The dashed lines in (a) represent the surface trace of extracted 2-D profiles shown in Fig. 14. The lowering opacity black curves feature the main structures in the region. White dashed rectangles in (d) feature the areas described in Fig. 10.

Figure 13 shows a slice at 300 m depth zoomed in the Alpes-Maritimes district and the city of Nice and illustrates the low velocity anomaly characteristics of the sedimentary basins around the Var and the Paillon rivers. The density of stations in the area provides a quite sufficient resolution to allow retrieving velocities which correlate with local geology.

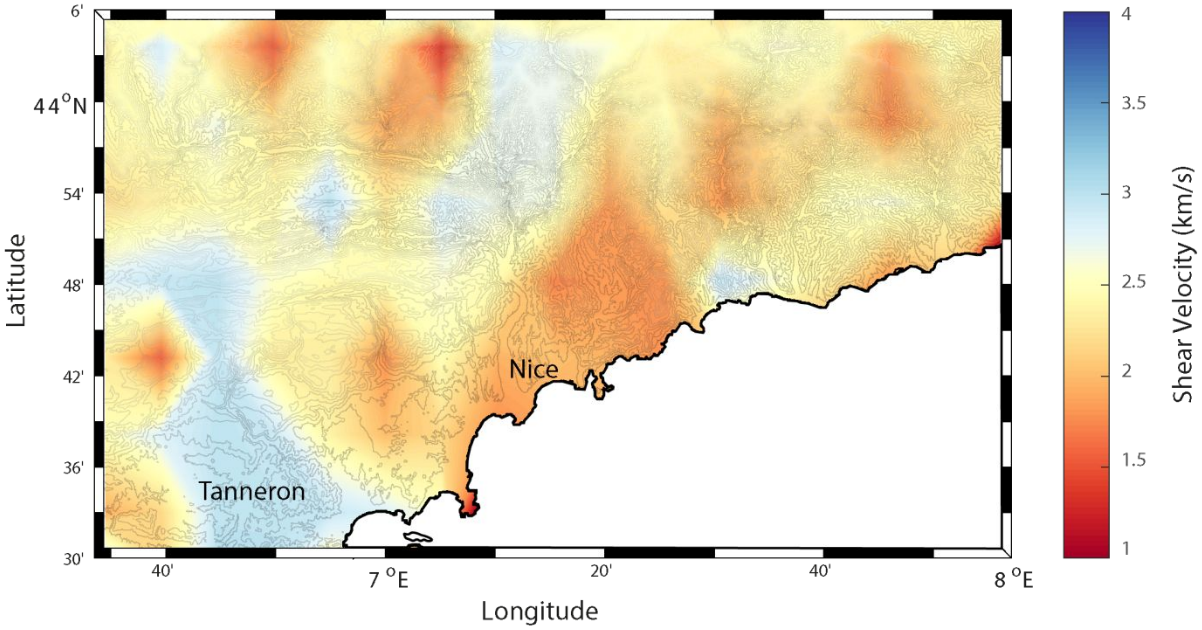

Figure 13. Depth slice through the 3-D final shear-velocity model, at 300 m, focused on the Alpes-Maritimes district.

In Figure 14, we show three 2-D profiles highlighting the main structures in the area. Profile P3 (west-east section) is aligned along the coast from the Maures massif to the Ligurian sea. Profiles P1 and P2 (north-south sections) highlight topographic between inland massifs and the margin/basin system.

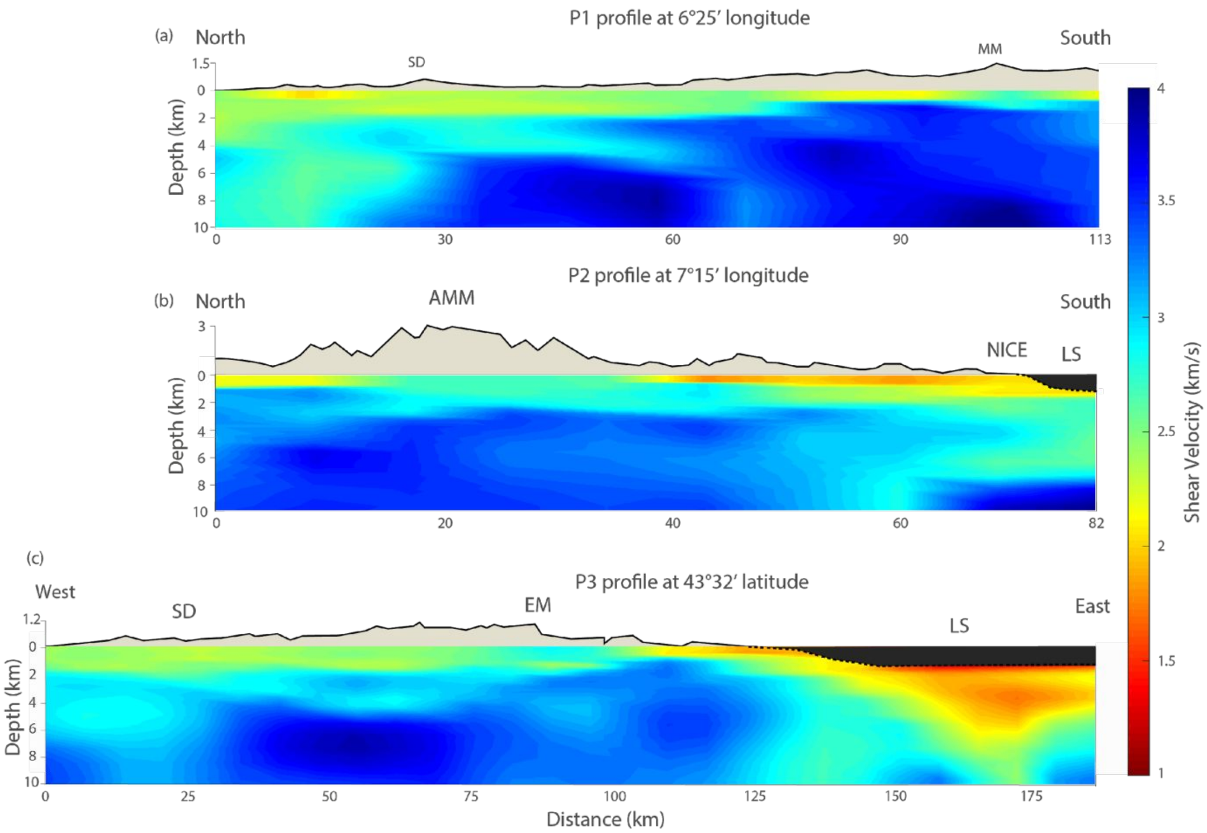

Figure 14. Vertical profiles P1, P2, P3 as mapped in Fig. 12, with same labels for toponyms and areas. Grey color features the Ligurian Sea.

4. Interpretation and discussion

Although recent surface wave tomography studies covering the south-western Alps were performed using the dense and large Alparray network, they cover the whole Alpine continental collision zone to obtain information in the crust and the upper mantle (Kästle et al., 2018, Lu et al. 2018). In this study, we opted to focus on the shallow crust, down to 10 km depth, where most of the seismicity is occurring in the region. Hence, a first comparison can be done on the Rayleigh and Love group velocity map at 8 s with the larger scale Alpine tomography. We found Rayleigh wave group velocity to be above 2.8 km/s on average and Love wave velocity group above 3 km/s which are consistent with velocities reported by Kästle et al. (2018) and Lu et al. (2018).

At depth ranging from 20 to 30 km depth, radial anisotropy was observed by Fry & al. (2010) in the orogen-parallel fast direction related to pre-alpine orogenic episode. However, at this regional scale and at shallower depth, no strong lateral variations of the radial anisotropy were identified from the comparison of Rayleigh and Love group velocity. Therefore, in this study we did not invert for radial anisotropy.

By looking both our Rayleigh and Love group velocity maps below 4 s (Figures 6 and 7), we can identify several areas featuring specific velocity anomalies. Two high-velocity zones around 3 km/s: (1) in the south-western part from Toulon to the west of Nice, which corresponds, from west to east of the anomaly, to the succession of the Maures, Tanneron and Esterel (labelled MEM and T in Figure 1) crystalline rock formations, (2) in the north-eastern part of our covered zone, corresponding to the crystalline rock formations of Mercantour-Argentera massif (labelled AM in Figure 1), the Dora-Maira massif (labelled DMM in Figure 1) and the sedimentary cover of the internal alpine belt (labelled C in Figure 1).

Between those two high-velocity anomalies, we can identify a low-velocity one of ~2 km/s (Figure 7) from the city of Nice to Digne-les-Bains, along the north-western part of the covered zone. This area corresponds to the external zone of south-western Alps called subalpine domain (labelled B in Figure 1). We retrieve this velocity anomaly up to 5 s periods on the Rayleigh group velocity maps (Figure 7). The thick sedimentary cover in this area can explain this low-velocity anomaly. By looking the Love group velocity maps (Figure 8), even if it's less obvious we can also identify this low velocity anomaly up to 3 s periods. However, a clearly visible low-velocity zone is retrieved centered on 44°N – 6°E from 3 to 5 s periods which corresponds to the position of the Plio-Quaternary Durance-Valensole basin (labelled DVB in Fig. 1).

When focusing on Nice area, which has the highest density of stations, and for periods below 3 seconds, we can clearly identify a low velocity-zone, visible on both Rayleigh and Love wave group velocity maps between 1.5 and 4 sec periods. At periods less than 2 s, much lower surface wave velocities are seen in this area. These areas consist of small sedimentary basins having sediments (alluvial, conglomerate and limestone aquifers) layers of several hundred meters like the Var valley (labelled V in Fig. 1) and the Paillon valley, located in the city of Nice (labelled N in Fig. 1). In the depth slices maps at 300 m (Figure 12), we distinctly observe the same pattern of low velocity around this area. This distribution of velocity is also visible in the N-S profile P2 (Figure 13b) down to 1 km depth from the coast to hinterland of Nice, an area known as Nice fold and thrust belt. Given the number of stations in this area, the resolution is maximum and allows us to locate superficial structures. At longer periods, between 5 and 9 s, the waves meet the crystalline substratum which is visible on the maps, as the velocity contrast with surrounding zones vanishes.

Lastly, the lowest-velocity anomaly retrieved, visible throughout the whole periods, corresponds to the east Ligurian margin showing ~1.5 km/s Scholte group-velocity wave. The ~2.3 km/s velocity retrieved just opposite Toulon can be explained by the fact that ASEAF station is located at the bottom edge of the continental slope, so that the surface waves, at the period considered, are not very sensitive to the superficial part filled with water, unlike OBSs found in the eastern part. Overall, the quality of the OBSs' GF retrieved, especially at short periods, and the lack of station in this area make interpretation more difficult when looking at the east Ligurian margin. Many studies exist in the Ligurian Basin since some of the largest seismicity in the region is located there. Dessa et al., (2011) highlighted a first layer from the sea bottom (2.4km) to 5 km depth with a P-wave velocity around 1.7 km/s down to 2 km/s, then a gradual increase in velocity from 2.8 km/s to 8 km depth. Using a Vp/Vs ratio of 1.7321, we find coherent low velocity anomalies in the vertical cross-sections and depth slices maps of the shear-wave velocity distribution compared to the ones observed by Dessa et al., (2011) (Figure 11 and 13). Our observations highlight the presence of this low-velocity zone down to ~6 km depth, which is linked to the presence of Salt and Evaporites from Plio-Quaternary deposits (Contrucci et al., 2001). In the eastern part, Lardeaux et al. (2006) identified P-wave velocities around 3.2 km/s at depth greater than 2 km, which is consistent with our shear-wave velocity model. Overall, the velocity anomaly retrieved below the 4 s group-velocity maps shows a good consistency with the major geological zones of the study area.

5. Conclusion

We used continuous three-component ambient noise recording obtained between 2011 and 2018 on 62 stations in the South-Western Alps and the Ligurian margin. By correlating the noise records between every station pairs, we retrieved Rayleigh and Love wave Green's functions and built 2-D group velocity maps and then a 3-D shear-velocity structure. The combined use of two depth inversions - first a Neighborhood algorithm for a coarse three layer models and then a linearized finite element approach - allowed us to observe distinctive velocity consistent with the surface geology. Most of the velocity variations are observed below 5 s. The 3D shear velocity profiles highlight the thinning of the sedimentary complex above massifs, and conversely, its thickening in the subalpine domain, in the north-west of the area, and in the sedimentary basins located between the Esterel massif and the Dora-Maira massif on the Italian side. The low velocity zone identified under the Ligurian Sea down to ~ 6 km depth is consistent with previous studies focusing on this part of the Ligurian Sea.

Given that most of the seismicity takes place in the Ligurian sea, a denser seismic network of broad-band sensors off shore of Nice could be useful to increase the area coverage at low period.

Acknowledgements

The authors acknowledge the POSA group for providing funding and data. The authors acknowledge the Alparray group work E. Bertrand from Cerema for providing CASSAT and SISVAR data. We thank Mr. and Mrs Metris for providing a quiet place to install one of the temporary station.

References

AlpArray Seismic Network (AASN) temporary component. AlpArray Working Group. Other/Seismic Network. doi:10.12686/alparray/z3_2015

Barmin, M., M. Ritzwoller, and A. Levshin (2001), A fast and reliable method for surface wave tomography, *Pure Appl. Geophys.*, **158**(8), 1351–1375.

Bensen, G.D., Ritzwoller, M.H., Barmin, M.P., Levshin, A.L., Lin, F., Moschetti, M.P., Shapiro, N.M. and Yang, Y. (2007), Processing seismic ambient noise data to obtain reliable broad-band surface wave dispersion measurements, *Geophys. J. Int.,* **169,** 1239–1260.

Béthoux, N., Fréchet, J., Guyoton, F., Thouvenot, F., Cattaneo, M., Eva, C., Nicolas, M. and Granet, M. (1992), A closing Ligurian Sea? *Pure and Applied Geophysics,* **139** (2), 179–194.

Béthoux, N., Tric, E., Chery, J. and Beslier (2008), Why is the Ligurian basin (Mediterranean Sea) seismogenic? Thermomechanical modeling of a reactivated passive margin. Tectonics.

Bigot-Cormier, F., Poupeau, G., Sosson, M., (2000), Dénudations différentielles du massif externe alpin de l'Argenetra (Sud-Est de la France) révélée par thermochronologie traces de fission (apatites, zircons). *Comptes Rendus de l'Académie des Sciences de Paris*, **330**, 363–370.

Chamoot-Rooke, N., Gaulier, J.M., Jestin, F., (1999), Constraints on Moho depth and crustal thickness in the Liguro–Provençal basin from 3D gravity inversion: geodynamic implications. In: Durand,B., et al. (Ed.). In the MediterraneanBasins: Tertiary Extension within the Alpine Orogen. *Geological Society of London Special Publication*, **vol. 156**, pp. 37–62.

Contrucci I., Nercessian A., Béthoux N., Mauffret A. and Pascal G., (2001), A Ligurian (Western Mediterranean Sea) geophysical transect revisited, *Geophysical Journal International*, **146**, Issue 1, Pages 74–97.

Dercourt, J., Zonenshain, L.P., Ricou, L.E., Kasmin, V.G., Le Pichon, X., Knipper, A.L., Grandjacquet, C., Sbortshikov, I.M., Geyssant, J., Lepvrier, C., Pechersky, D.H., Boulin, J., Sibuet, J.C., Savostin, L.A., Sorokhtin, O., Westphal, M., Bazhenov, M.L., Lavez, J.P. and Biju-Duval, B. (1986), Geological evolution of the Tethyan belts from Atlantic to Pamirs since the Lias. *Tectonophysics,* **123**, 241–315.

Dessa, J.X., Soazig S., Marjorie L., Marie-Odile B., Anne D., Nicole B., Stefano S., Françoise S., Elena E., Gabriele F., Olivier B. and Claudio E, (2011), The GROSMarin experiment: three-dimensional crustal structure of the North Ligurian margin from refraction tomography and preliminary analysis of microseismic measurements. *Bulletin de la Société Géologique de France*, **182** (4): 305–321.

Dewey, J., Helman, M., Turco, E., Hutton, D. and Knott, S. (1989), Kinematics of the western Mediterranean. In: Coward, M., Dietrich, D., Parks, G.G. (Eds.), Alpine Tectonics. *Geological Society of London Special Publicatio*n, **45**, pp. 265–283.

Faccenna, C., Mattei, M., Funicello, R., Jolivet, L., (1997), Styles of back-arc extension in the Central Mediterranean. *Terra Nova*, **9**, 126–130.

Fry, N., (1989), Southwestward thrusting and tectonics of the western Alps.In: Coward, M., Dietrich, D., Park, R.G. (Eds.), Alpine Tectonics. *Geolological Society of London Special Publication*, **vol. 45**, pp. 83–109.

Fry B., Deschamps F., Kissling E., Stehly L. and Giardini D., (2010), Layered azimuthal anisotropy of Rayleigh wave phase velocities in the European Alpine lithosphere inferred from ambient noise, *Earth planet. Sci. Lett.,* **vol.297** (pg.95-102).

Gattacceca J., Deino A., Rizzo R., Jones D.S., Henry B., Beaudoin B. and Valeboin F., (2007), Miocene rotation of Sardinia: new paleomagnetic and geochronological constraints and geodynamic implications, *Earth planet. Sci. Lett.*, **258**, 359–377.

Giannopoulos D., Rivet D., Sokos E., Deschamps A., Mordret A., Lyon-Caen H., Bernard P., Paraskevopoulos P. and Tselentis G.A. (2017), Ambient noise tomography of the western Corinth Rift, Greece, *Geophysical Journal International*, **211**, 284–299.

Haney M.M. and Tsai V.C. (2017), Perturbational and nonperturbational inversion of Rayleigh-wave velocities. *Geophysics*, **82**(3), F15-F28.

Hetenyi, G., Molinari, I., Clinton, J., and al., (2018), The AlpArray Seismic Network: A large-scale European experiment to image the Alpine orogen, *Surv. Geophys.,* **39***,* 1009-1033.

Ioualalen, M., Larroque, C., Scotti, O. and Daubord, C., (2014), The tsunami coastal distribution and hazard along the French–Italian Riviera. *Pure Appl. Geophys.* **171**, 1423–1443.

INGV Seismological Data Centre. (1997). Rete Sismica Nazionale (RSN). Istituto Nazionale di Geofisica e Vulcanologia (INGV), Italy. http://doi.org/10.13127/SD/X0FXnH7QfY

Jolivet, L., Augier, R., Faccenna, C., Negro, F., Rimmele, G., Agard, P., Robin, C., Rossetti, F. and Crespo-Blanc, A.C., (2008), Subduction, convergence et extension arrière-arc en Méditerranée. *Bull. Soc. Geol. Fr.* **179** (6), 525–550.

Kastle, E. D., El-Sharkawy, A., Boschi, L., Meier, T., Rosenberg, C., Bellahsen, N. and Weidle, C. (2018), Surface wave tomography of the Alps using ambient-noise and earthquake phase velocity measurements. *Journal of Geophysical Research: Solid Earth,* **123**, 1770–1792.

Köhler, A., Weidle, C. and Maupin, V. J. (2012), On the effect of topography on surface wave propagation in the ambient noise frequency range. *Journal of Seismology,* **16**: 221.

Lardeaux, J.M., Schwartz, S., Tricart, P., Paul, A., Guillot, S., Béthoux, N. and Masson, F, (2006), A crustal-scale cross-section of the south-western Alps combining geophysical and geological imagery. *Terra Nova.* **18**. 412 - 422.

Larroque, C., Béthoux, N., Calais, E., Courboulex, F., Deschamps, A., Déverchère, J., Stéphan, J.F., Ritz, J.F., Gilli, E., 2001. Active deformation at the junction between southern French Alps and Ligurian basin. *Netherlands Journal of Geosciences/Geologie en Mijnbouw* **80** (3–4), 255–272.

Larroque, C., Delouis, B., Godel, B. and Nocquet, J.-M. (2009), Active deformation at the southwestern Alps–Ligurian basin junction (France–Italy boundary): Evidence for recent change from compression to extension in the Argentera Massif. *Tectonophysics*. **467**. 22-34.

Larroque C., Oona S. and Mansour I. (2012), Reappraisal of the 1887 Ligurian earthquake (western Mediterranean) from macroseismicity, active tectonics and tsunami modelling, *Geophysical Journal International*, **190**, Issue 1, 87–104.

Larroque, C., & Scotti, O., Ioualalen M., Migeon S., Virginie H., and Bernard d.L., (2014). The February 23, 1887: a Mw 6.7-6.9 earthquake with induced tsunami and submarine slide on the Ligurian coast (western Mediterranean).

Laurent, O., Stéphan, J.F., Popoff, M., 2000. Modalités de la structuration miocène de la branche sud de l'arc de Castellane (chaînes subalpines méridionales). *Géologie de la France*. **3**, 33–65.

Levshin, A., Yanovskaya, T., Lander, A., Bukchin, B., Barmin, M., Ratnikova, L. and Its, E. (1989), Recording, identification, and measurement of surface wave parameters, in *Seismic Surface Waves in a Laterally Inhomogeneous Earth*, pp. 131–182, ed. Keilis-Borok, V.I., Kluwer.

Lin, F.C, Moschetti, M.P. and Ritzwoller, M.H. (2008), Surface wave tomography of the western United States from ambient seismic noise: Rayleigh and Love wave phase velocity maps, *Geophysical Journal International*, **173**, 281–298.

Lu, Y., Stehly, L., Paul, A., and AlpArray Working Group (2018), High-resolution surface wave tomography of the European crust and uppermost mantle from ambient seismic noise. *Geophysical Journal International*, ***214***(2), 1136-1150.

Malinverno, A., Ryan, W.B.F., (1986), Extension in the Tyrrhenian Sea and shortening in the Apennines as a result of arc migration driven by sinking of the lithosphere. *Tectonics*, **5**, 227–245.

Masson, F., Verdun, J., Bayer, R., Debeglia, N., (1999), Une nouvelle carte gravimétrique des Alpes occidentales et ses conséquences structurales et tectoniques. *Comptes Rendus de l'Académie des Sciences de Paris*, **329**, 865–871.

Mordret, A., Landès, M., Shapiro, N.M., Singh, S., Roux, P. and Barkved, O. (2013), Near-surface study at the Valhall oil field from ambient noise surface wave tomography, *Geophys. J. Int.,* **193**(3), 1627–1643.

Mordret, A., Landès, M., Shapiro, N., Singh, S., and Roux, P. (2014), Ambient noise surface wave tomography to determine the shallow shear velocity structure at Valhall: Depth inversion with a Neighbourhood Algorithm, *Geophys. J. Int.*, ***198***(3), 1514–1525.

Mordret, A., Rivet, D., Landès, M. and Shapiro, N.M. (2015), 3-D shear velocity anisotropic model of Piton de la Fournaise volcano (la Réunion island) from ambient seismic noise, *J. geophys. Res.,* **120**(1), 406–427.

Nocquet, J.-M. (2012). Present-day kinematics of the Mediterranean: A comprehensive overview of GPS results. *Tectonophysics*. **579**. 220–242.

Nunn, C., and al. (2014b), Imaging the lithosphere beneath NE Tibet: Teleseismic P and S body wave tomography incorporating surface wave starting models, *Geophys. J. Int.,* **196**(3), 1724–1741.

Rawlinson, N., and Sambridge, M. (2004), Wavefront evolution in strongly heterogeneous layered media using the fast marching method, *Geophys. J. Int.*, **156**(3), 631–647.

Réhault, J.P., Boillot, G., Mauffret, A., 1984. The western Mediterranean basin geological evolution. *Marine Geology*, **55**, 447–477.

RESIF-RLBP French Broad-band network, RESIF-RAP strong motion network and other seismic stations in metropolitan France. RESIF - Réseau sismologique & géodésique français. http://doi.org/10.15778/RESIF.FR

Riccou, L.E., Siddans, A., (1986). Collision tectonics in the western Alps. In: Coward, M., Ries, A.C. (Eds.), Collision Tectonics. *Geolological Society of London Special Publication,* **vol. 19**, pp. 229–244.

Ritzwoller, M. H., Lin F.-C., and Shen W. (2011), Ambient noise tomography with a large seismic array, *C. R. Geosci.*, **343**(8), 558–570.

Rollet N., Déverchère J., Beslier M.O., Guennoc P., Réhault J.P., Sosson M. and C. Truffert (2002), Back arc extension, tectonic inheritance and volcanism in the Ligurian sea, *Western Mediterranean. Tectonics,* **21**.

Sanchez, G., Rolland, Y., Corsini, M., Jolivet, M., Brichaud, S. and Carter, A., (2011), Exhumation controlled by transcurrent tectonics: the Argentera-Mercantour massif (SW Alps). *Terra Nova* 00, 1–11.

Sambridge, M. (1999a), Geophysical inversion with a neighborhood algorithm – I. Searching a parameter space, *Geophys. J. Int.,* **138**(2), 479–494.

Sambridge, M. (1999b), Geophysical inversion with a Neighbourhood Algorithm – II. Appraising the ensemble, *Geophys. J. Int.,* **138,** 727–746.

Schreiber D., Lardeaux J.M., Martelet G., Courriou G. and Guillen A., (2010), 3-D modelling of Alpine Mohos in Southwestern Alps, *Geophys. J. Int.*, **180**, 961–975.

Séranne, M., (1999), The Gulf of Lions continental margin (NW Mediterranean) revisited by IBS: an overview. In: Durand, B., Jolivet, L., Horvath, F., Séranne, M. (Eds.), On the Mediterranean Basins: Tertiary within Alpine Orogen. *Geological Society of London*, Special Publication, **vol. 156**, pp. 15–36.

Stehly L., Fry B., Campillo M., Shapiro N. M., Guilbert J., Boschi L. and Giardini D. (2009), Tomography of the Alpine region from observations of seismic ambient noise, *Geophysical Journal International*, **178**, 338–350.

Schippkus, S., Zigone,D., Bokelmann, G. and the AlpArray Working Group (2018), Ambient-noise tomography of the wider Vienna Basin region, *Geophysical Journal International*, **215**, 102–117.

Thouvenot, F., Paul, A., Fréchet, J., Béthoux, N., Jenatton, L., Guiguet, R., (2007), Are there really superposed Mohos in the south-western Alps? New seismic data from fan-profiling reflections. *Geophysical Journal International*, **170**,1180–1194.

Tricart, P., (1984), From passive margin to continental collision: a tectonic scenario for the western Alps. *American Journal of Science*, **284**, 97–120.

Westphal M., Orsini J. and Vellutini P., (1976), Le microcontinent corso-sarde, sa position initiale, données paléomagnétiques et raccords géologiques, *Tectonophysics*, **30**, 41–57.